Recrystallization of Hot-Rolled 2A14 Alloy During Semi-Solid Temperature Annealing Process

Yingze Liu , Jufu Jiang * , Ying Zhang , Minjie Huang , Jian Dong , Ying Wang *

Posted Date: 27 February 2023

doi: 10.20944/preprints202302.0436.v1

Keywords: semi-solid annealing; 2A14 aluminum alloy; hot-rolled; EBSD; TEM; recrystallization

Article

Recrystallization of Hot-Rolled 2A14 Alloy during Semi-Solid Temperature Annealing Process

Yingze Liu [1], Jufu Jiang [2,*], Ying Zhang [1], Minjie Huang [1], Jian Dong [1] and Ying Wang [2,*]

[1] School of Materials Science and Engineering, Harbin Institute of Technology, Harbin, 150001, P.R. China
[2] School of Mechatronics Engineering, Harbin Institute of Technology, Harbin, 150001, P.R. China
* Correspondence: author: J.J. jiangjufu@hit.edu.cn; Tel. +86-18746013176; Y.W. wangying1002@hit.edu.cn; Tel. +86-15945697615

Abstract: In this paper, in order to provide proper parameters for the preparation of semi-solid billets, the semi-solid annealing of hot-rolled 2A14 Al alloy was investigated. The microstructure was characterized by X-ray diffraction (XRD), scanning electron microscope (SEM) with X-ray energy dispersive spectrometer (EDS) and electron backscattered diffraction (EBSD), scanning transmission electron microscope (STEM). XRD results show that with the increase of temperature, equilibrium θ-Al2Cu gradually dissolved in the matrix. The EDS results of SEM and STEM show that there were coarse θ-Al2Cu phase, ultra-fine precipitate Al(MnFeSi) or (Mn, Fe)Al6 phase and atomic clusters in the microstructure. EBSD results show that the recrystallization mechanism was dominated by continuous static recrystallization (CSRX), the homogeneous nucleation occurred when the sample was heated to near solidus temperature, and CSRX happened in the semi-solid temperature. In the process of recrystallization, the micro-texture changed from preferred orientation to random orientation. A variety of experimental results show that static recrystallization (SRX) occurred at semi-solid temperature due to the blocking effect of atomic clusters on dislocation slip and the Zener drag effect of fine precipitates on low angle grain boundaries (LAGBs) disappeared with melting at semi-solid temperature.

Keywords: semi-solid annealing; 2A14 aluminum alloy; hot-rolled; EBSD; TEM; recrystallization

1. Introduction

Aluminum alloys are still enduring in the field of aerospace with excellent comprehensive mechanical properties and unparalleled economic applicability, even in the face of competition from magnesium alloys, titanium alloys and composites [1–3]. In addition to improving the alloy composition, the innovation of thermomechanical processing (TMP) is also important. Reasonable TMP can not only save materials and reduce costs, but also help to make the reasonable distribution of polycrystalline texture and achieve the purpose of strengthening mechanical properties. Semi-solid metal processing (SSM) is a mature metal near net shape forming technology [4]. It is widely used in the forming of complex shape aluminum alloy parts. The key step in SSM is to prepare semi-solid billets. Strain induced melt activation (SIMA) method and the recrystallization and partial melting (RAP) method are two traditional method to fabricating semi-solid billets [5]. The method of preparing semi-solid billet can be summarized as pre-deformation (PD) of the material, and then semi-solid isothermal treatment (SSIT) to prepare semi-solid billet. According to different PD method, several semi-solid billet preparation methods are derived [5]. Binesh and Aghaie-Khafri [6] introduced repetitive upsetting extrusion (RUE) method as PD to modified SIMA, increasing the microstructure of semi-solid 7075 alloy. Fu et al. [7] investigated the coarsening behaviors of 7075 aluminum alloy during equal channel angular pressing (ECAP) based SIMA method. The introduction of severe plastic deformation (SPD) as pre-deformation method for preparing semi-solid billet is helpful to refine the grain of semi-solid billet, but it also complicates the process and increases the cost. In this paper, to simplify the semi-solid billet preparation processing, the commercial hot-rolled 2A14 thick plate was used for original material. Instead of additional deformation processing, it was directly subjected to SSIT. This method was called wrought aluminum alloy directly semi-solid thermal treatment (WADSSIT) method [8].

Because the excellence mechanical performance and structural carrying capacity, good weldability, 2A14 aluminum alloys are served as the material for key structural parts of the aircrafts such as wheels and holders with complex shape [9]. Lan et al. [9] founded that cold deformation prior to artificial aging will promote the precipitation of phases θ'', θ' and θ (Al_2Cu) in 2A14 alloy, so as to shorten the peak aging time. Wang et al. [10] investigated the multidirectional forging (MDF) on 2A14 aluminum alloy, transmission electron microscopy (TEM) results revealed that second phase particles dynamic precipitated during deformation can inhibit dislocation motion thus increased the yield strength of the alloy. Wang et al. [11] founded that higher MDF temperatures increased the solubility and diffusion efficiency of the solute atoms, resulting in fine and spherical second phases particles, which improved the mechanical properties. The research on 2A14 alloy focused on forging [9–11], but there was no report on SSM in 2A14 alloy. For parts with complex shapes, SSM has the advantages of saving raw materials and reducing the cost of subsequent machining. In addition, researches on SSM focused more on 7xxx series aluminum rather than 2xxx series aluminum alloy [7,12–14]. However, different series of aluminum alloys have significant differences in phase composition, semi-solid range and recrystallization mechanism. Therefore, it is significant to investigate the SSM of 2A14 alloy.

Recrystallization phenomenon occurs in various TMPs [15]. It has an important influence on the microstructure, texture evolution and properties of various TMPs [16]. Recrystallization also plays an important role in the preparation of semi-solid billets. In the pre-deformation stage, dynamic recrystallization (DRX) may take place, so that the deformation energy is stored in the material in the form of high (HAGBs) and low angle grain boundaries (LAGBs). In the temperature rising stage of SSIT, static recrystallization (SRX) may occur, the deformed grains turns into uniform equiaxed grains. Generally, discontinuous static recrystallization (DSRX) may occur during SSIT with clear no-deformation nuclei formation and growth [6,14,17]. SRX can also take place homogeneously without clear nucleation and growth stage, and is labelled as continuous static recrystallization (CSRX). CSRX is a common phenomenon in particle-stabilized subgrain structure aluminum alloy [18]. However, there is no report on CSRX in the process of semi-solid preparation. On the one hand, because the research focus of semi-solid billet preparation is often on grain refinement, roundness and microstructure coarsening behavior, the recrystallization behavior in the temperature rising process is often ignored [14,19]. On the other hand, increasing the degree of pre-deformation to refine the microstructure is also a more common research method, which may affect the occurrence of CSRX. The SRX behavior will affect the coarsening behavior, texture, which provides technical guidance for the preparation of semi-solid billets. Therefore, it is necessary to study the recrystallization behavior in the temperature rising stage.

Electron backscatter diffraction (EBSD) combined with software such as channel 5 or Mtex is suitable for the characterization of polycrystalline materials. Kernel average misorientation (KAM), grain reference orientation deviation (GROD), grain orientation spread (GOS) are powerful tools to characterize the recrystallization behavior. Orientation distribution function (ODF) can characterize the micro-texture of the corresponding scanning area. However, EBSD is limited by the resolution range of its coupled scanning electron microscope, and cannot characterize the interaction between dislocation and precipitated particles. Transmission electron microscope (TEM) can tackle this problem. In this paper, the SRX behavior and micro-texture of 2A14 Al alloy in the temperature rising stage during WADSSIT was investigated systemically through EBSD and TEM technology. The reason of CSRX and the effect of CSRX on spheroidization and coarsening in SSIT process are discussed.

2. Materials and Methods

2.1. Starting material

The wrought 2A14 aluminum alloys used in this study were purchased from the Northeast Light Alloy Co., Ltd of China. The supply status was hot rolled medium-thick plate of 50mm with a cumulative deformation of 90% at 400 ℃. The chemical composition was tested by X-ray fluorescence

Preprints (www.preprints.org) | NOT PEER-REVIEWED | Posted: 27 February 2023 doi:10.20944/preprints202302.0436.v1

(XRF) as shown in Table 1. As shown in Figure 1, the semi-solid temperature ranged from 512 ℃ to 663 ℃ as tested via differential scanning calorimetry (DSC, STA449F3). The scanning speed is 10 ℃ /min. The solid fraction f_s was determined by Eq. (1)

$$f_s(T) = 1 - \left[\frac{(H-H_{solidus})-C_p\cdot(T-T_{solidus})}{(H_{liquidus}-H_{solidus})-C_p\cdot(T_{liquidus}-T_{solidus})}\right], \quad (1)$$

where H is the enthalpy, T is the temperature, C_p is the heat capacity of the alloy, L is the latent heat of fusion. The solid fraction vs. temperature curve is shown in Figure 1.

Table 1. Chemical composition of 2A14 aluminum alloy (wt.%).

Element	Cu	Si	Mn	Mg	Fe	Ti	Zn	Ni	Al
Standard	3.9~4.8	0.6~1.2	0.4~1.0	0.4~0.8	⩽0.7	⩽0.15	⩽0.3	⩽0.1	Bal.
Sample	4.370	0.916	0.781	0.590	0.177	0.025	0.027	0.006	Bal.

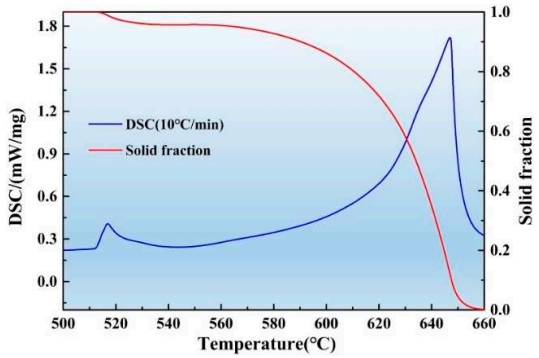

Figure 1. Semi-solid range and solid fraction – temperature curve of 2A14 Al alloy.

2.2. Recrystallization process

The WADSSIT method was used to fabricate semi-solid billets of 2A14 alloy. It has the temperature rising stage and the temperature holding stage, as shown in Figure 2. The recrystallization process was occurred during the temperature rising stage. The 8 × 10 × 12 mm^3 cuboid samples were cut from the hot-rolled plate, and rolling direction (RD), normal direction (ND), transverse direction (TD) were distinguished by the side length of the sample. The samples were continuous heating from room temperature to the given temperatures in a muffle furnace. When the temperature reached to 480 ℃, 505 ℃, 530 ℃, 555 ℃, 580 ℃, 600 ℃ or 620 ℃, the samples were quenched in cold water immediately to freeze the microstructure. In the temperature holding stage, the holding time was set to 5 min, 10 min, 15min, 20 min, 25 min and 30min.

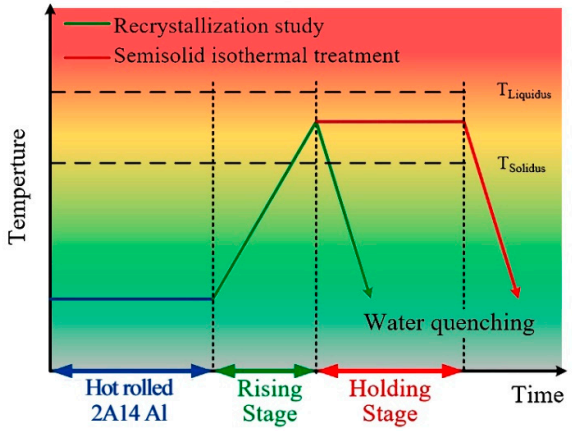

Figure 2. Schematic illustration of the WADSSIT process.

2.3. Characterization of microstructure

For the optical microscopy (OM) observation, the equipment used was Olympus GX71. The samples were ground with 100, 400, 800, 1000 and 2000 grit papers and then polished on a gold velvet disc sprayed with 1 μm diamond powder at 1200 rpm for 5 min, and finally chemically etched with Keller's reagent. The chemical composition of the Keller's reagent was an aqueous solution with 2.5%HNO_3, 1.5%HCl, and 1%HF, the etching time was 25s.

For the EBSD characterization, the equipment used was Zeiss Supra 55 scanning electron microscope (SEM) equipped with EBSD function and X-ray energy dispersive spectrometer (EDS). The samples underwent the same ground and mechanical polishing method with the OM samples. Then, in order to remove the influence of the pseudo stress layer introduced by mechanical polishing on the EBSD test, the samples were ion polishing using Leica RES101 with the voltage of 6.5 V and polishing time of 1 h. In order to obtain as accurate EBSD information as possible, the scanning step was set to 2 microns, and the scanning range of each sample was set to 470×350=164500 scanning points. Channel 5 and Mtex analysis softwares were used to analyze the EBSD data.

For the transmission electron microscope (TEM) characterization, the equipment used was FEI Talos F200X. The samples were cut to 300 μm thickness by wire cutting. Then the samples were polished to a thickness of 30 μm with 2000 grit SiC sandpaper and a screw micrometer. Then punched out 3 mm diameter discs from the samples with a punch. The discs were etched by argon-ion with a precision ion polishing system (Gatan 695) to a thickness of about 100 nm.

3. Results

3.1. Microstructure of the raw material

Figure 3(a)-(c) shows the OM images of the hot-rolled plate on ND-RD plane, TD-ND plane and TD-RD plane, respectively. The schematic diagram of hot-rolled plate direction are shown in Figure 3(d). As the accumulated deformation in the hot rolling process reached 90%, the DRX occurred under hot large plastic deformation, resulting in a large number of dislocation entanglements and LAGBs. There were a lot of defects in the crystal, which made the energy in the crystal close to that at the grain boundary. Therefore, it is difficult to distinguish the grain boundary contrast etched by the Keller's reagent under the optical microscope. However, due to the different grain orientation, the corrosion resistance was different, and the contrast of some grains could be distinguished. In Figure 3(a), the grains were elongated along the RD. In Figure 3(b), the grain contrast was almost invisible. In Figure 3(c), in addition to elongated grains along RD, there were also fine equiaxed grains with a size of about 50 microns. Due to the large cumulative deformation and limited by the analytical ability of the SEM-EBSD equipment used, the resolution of EBSD results of the raw material on the ND-RD, TD-RD plane were not satisfactory. In order to study the evolution of micro-texture and eliminate the analysis of pseudo results due to insufficient resolution, the EBSD test of raw material was carried out on TD-ND plane, and the EBSD-IPF results are shown in Figure 3(d). In MTEX software, set the LAGB threshold for identifying grains to 15 °, which was outlined by black lines. On the TD-ND plane, the microstructure was composed of huge elongated grains and fine small grains. In large grains, the color of IPF at different positions was different, indicating that there was a certain misorientation at different positions in the grains.

Preprints (www.preprints.org) | NOT PEER-REVIEWED | Posted: 27 February 2023 doi:10.20944/preprints202302.0436.v1

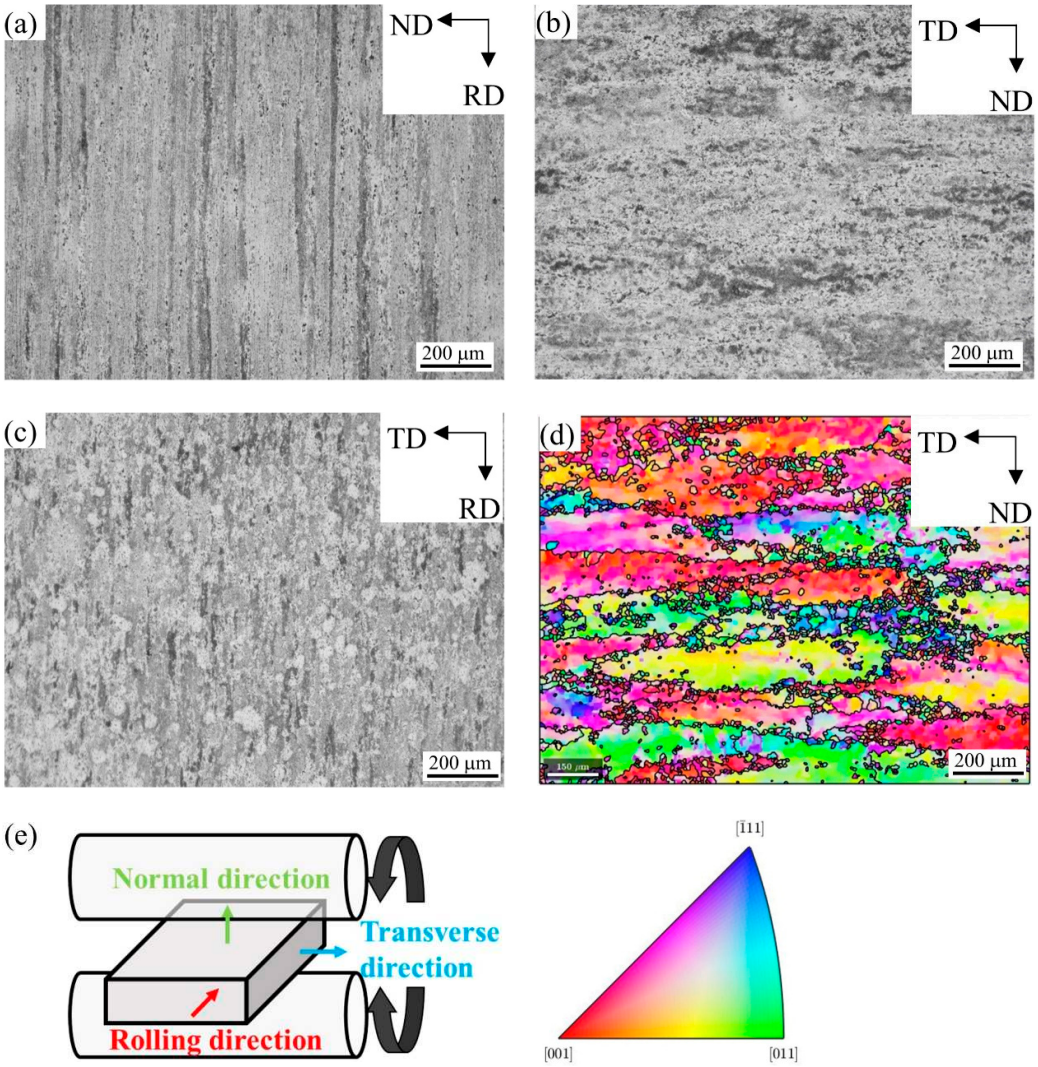

Figure 3. Microstructure of the raw hot-rolled 2A14 Al alloy on (**a**) ND-RD plane, (**b**) TD-ND plane, (**c**) TD-RD plane; (**d**) EBSD-IPF image of raw material on TD-ND plane; (**e**) schematic diagram of hot-rolled plate direction.

3.2. EBSD analysis results during recrystallization process

Figure 4 (a), (b) and (c) shows the EBSD-IPF images of 2A14 Al alloy on RD-TD plane annealing to 505 ℃, 555 ℃ and 580 ℃, respectively. The corresponding IPF grain orientation ruler is shown in Figure 4 (d). With the increase of annealing temperature, the grain size grew gradually. When annealing to 505 ℃ and 555 ℃, the color difference in a single grain was large, which indicates that there were still many defects in the grain, and LAGBs existed. When annealing to 580 ℃, the color in a single grain was relatively consistent, indicating that recovery and recrystallization occurred in the process of increasing the temperature, and the defects in the grain were gradually reduced.

Preprints (www.preprints.org) | NOT PEER-REVIEWED | Posted: 27 February 2023 doi:10.20944/preprints202302.0436.v1

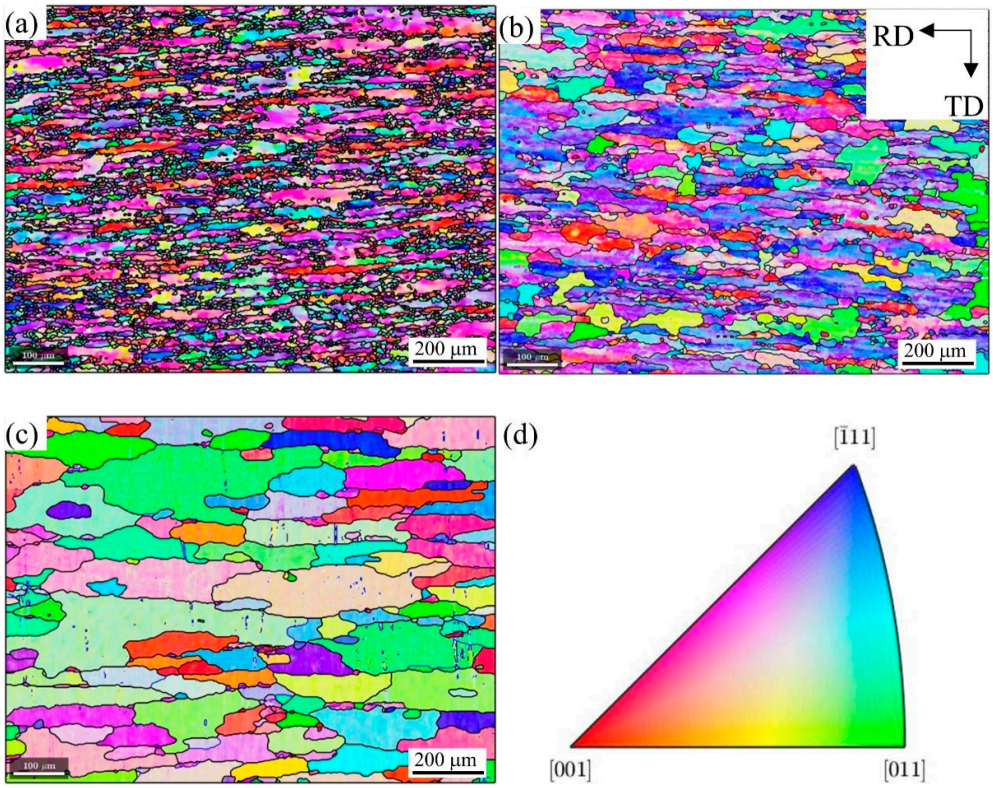

Figure 4. EBSD-IPF images of 2A14 Al alloy on RD-TD plane annealing to (**a**) 505 ℃, (**b**) 555 ℃, (**c**) 580 ℃; (**d**) IPF grain orientation ruler.

In order to further study the evolution of grain boundaries during recrystallization annealing, the grain boundaries diagram and grain boundaries density diagram on the RD-TD plane are drawn, as shown in Figure 5. Due to the limited resolution accuracy of EBSD test and the magnification of SEM, the threshold of LAGBs recognition was set to 2°, and the sub grain boundaries that less than 2° were ignored. When the annealing temperature reached 505 ℃ (Figure 5(a)), the microstructure was densely covered with LAGBs, the peak relative density of LAGBs reached 14, and the relative density of LAGBs in most areas was higher than 12 (Figure 5(d)). With the increase of annealing temperature to 555 ℃ (Figure 5(b)), the grain size became larger, in other words, the HAGBs became less. Some grains with low-density grain boundaries appeared in the structure, which indicates that the recovery phenomenon of the structure occurred along with the recrystallization process. The relative density peak of grain boundary was still 14, see Figure 5(e), while the relative density of grain boundary in most areas remained at a high level, and only low-density grain boundary areas appeared in local areas. With the increase of annealing temperature, the grain boundaries will migrate, and the migration of grain boundaries will reduce the density of grain boundary in the crystal. When annealing at 505 ℃, the migration of LAGBs was obviously blocked. With the increase of temperature to 555 ℃, the grain boundary density in some areas decreased, indicating that this hindrance was disappearing. When the annealing temperature reached 580 ℃ (Figure 5(c)), the grains grew further, and the LAGBs in the grains were greatly reduced to disappear. The grain boundary density figure (Figure 5(f)) shows that the peak relative density of grain boundary decreased to 1.4 at 580 ℃, which is one tenth of that in 505 ℃ and 555 ℃. At the same time, the relative grain boundary density in most areas was less than 1.

Preprints (www.preprints.org) | NOT PEER-REVIEWED | Posted: 27 February 2023 doi:10.20944/preprints202302.0436.v1

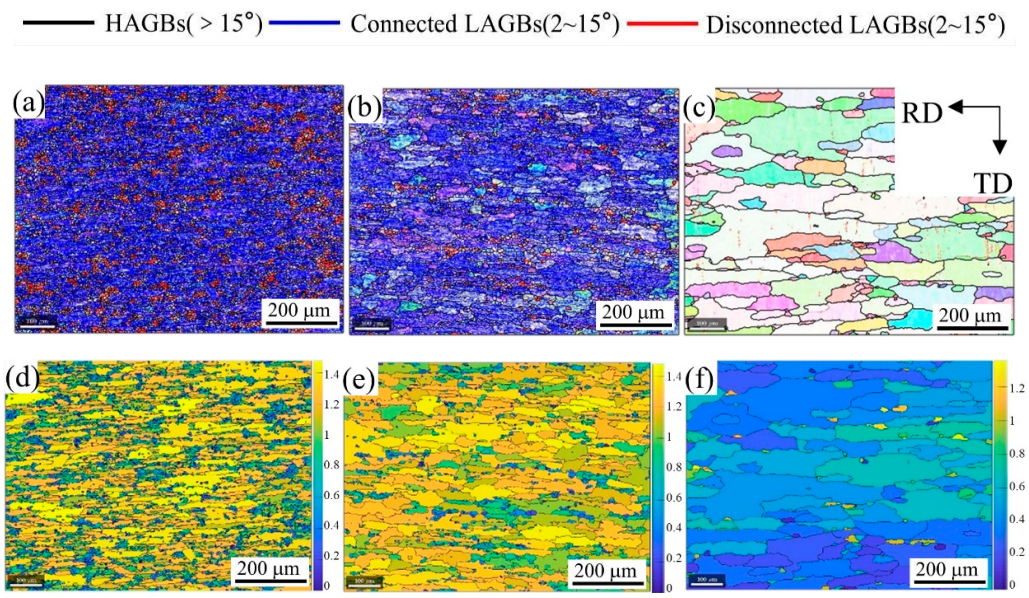

Figure 5. Grain boundaries images of 2A14 Al alloy on RD-TD plane annealing to (**a**) 505 ℃, (**b**) 555 ℃, (**c**) 580 ℃; Grain boundaries density images of 2A14 Al alloy on RD-TD plane annealing to (**d**) 505 ℃, (**e**) 555 ℃, (**f**) 580 ℃.

In the process of annealing, in addition to the evolution of grain boundaries, the evolution of dislocations is also an interesting phenomenon. Generally speaking, with the increase of annealing temperature, dislocations will slip and climb, different dislocations will annihilate, and the same dislocations will be directionally arranged to form dislocation walls (sub-grain boundaries). Due to the annihilation of different dislocations, the dislocation density will decrease, which is often called the metal recovery phenomenon. Unfortunately, the resolution scale of EBSD cannot reach the dislocation level, but the change trend of dislocation density can be qualitatively analyzed by theoretical calculation.

The kernel average misorientation results of 2A14 Al alloy on RD-TD plane annealing to 505 ℃, 555 ℃, 580 ℃ is shown in Figure 6 (a), (b), (c), respectively. When the annealing temperature reached 505 ℃ (Figure 6(a)), the peak value of KAM reached 15, and the KAM value in most areas was more than 10, indicating that the geometrically necessary dislocations (GNDs) density in the structure were high. With the increase of temperature to 555 ℃ (Figure 6(b)), the peak value of KAM was still 15, indicating that the GNDs density of the high-density dislocation regions were not decreased. The KAM value of most areas decreased to below 10, and some areas with KAM value lower than 5 appeared. Comparing with Figure 5(b) and (e), these low-density dislocation regions coincide with the low-density grain boundary regions. With the annealing temperature reached 580 ℃ (Figure 6(c)), the peak value of KAM decreased to 10, the KAM value of most areas decreased below 3, which shows that the GNDs density in most regions decreased, and only the GNDs density near the HAGBs was higher. The annihilation of reverse dislocations will reduce the dislocation density. In order to annihilation, dislocations need to slip and climb first. When annealed to 555 ℃, the dislocations in some regions could slip and annihilate to reduce the dislocation density and formed a low-density dislocation region. The decrease of KAM value in most areas was not obvious, indicating that the slip of dislocation was hindered. It is speculated that the slip of dislocation was hindered due to the existence of dispersed precipitation phase, which needs to be further confirmed by energy dispersive spectrum (EDS) test.

Apart from the evolution of dislocations, the recrystallization can also be characterized more intuitively by EBSD results. For each individual grain separated by the HAGBs, the average orientation of the grain can be obtained by calculating the orientation of each pixel in the grain. The orientation of each pixel has a deviation from the average orientation of the grain. The grain

Preprints (www.preprints.org) | NOT PEER-REVIEWED | Posted: 27 February 2023 doi:10.20944/preprints202302.0436.v1

orientation spread (GOS) value can be obtained by averaging the deviation of all pixels in the grain from the average orientation. Generally speaking, grains with GOS value below 1.8° were regarded as recrystallized grain structure, grains with GOS value between 1.8 and 3 were regarded as sub-grain structure, and grains with GOS value over 3 were regarded as deformed grain structure. The GOS figures of 2A14 Al alloy on RD-TD plane annealing to 505 ℃, 555 ℃ , 580 ℃ is shown in Figure 6 (d), (e), (f), respectively. When annealed to 505 ℃ (Figure 6(d)), the peak value of GOS reached 38, the GOS value of most grain regions exceeded 10, and the GOS value of almost all grains was higher than 3, indicating that it was a deformed structure at this time. When annealed to 555 ℃ (Figure 6(e)), the peak value of GOS decreased to 23, the GOS value of most grain regions decreased to 8, and the GOS value of some grain regions were lower than 3, indicating that some substructures appeared. When annealed to 580 ℃ (Figure 6(f)), the peak value of GOS decreased to 7, the GOS value of most grain regions were lower than 3, the GOS value of half the grain regions were lower than 1.8, indicating that the recrystallization has been basically completed, and there were a few substructures and deformed structures.

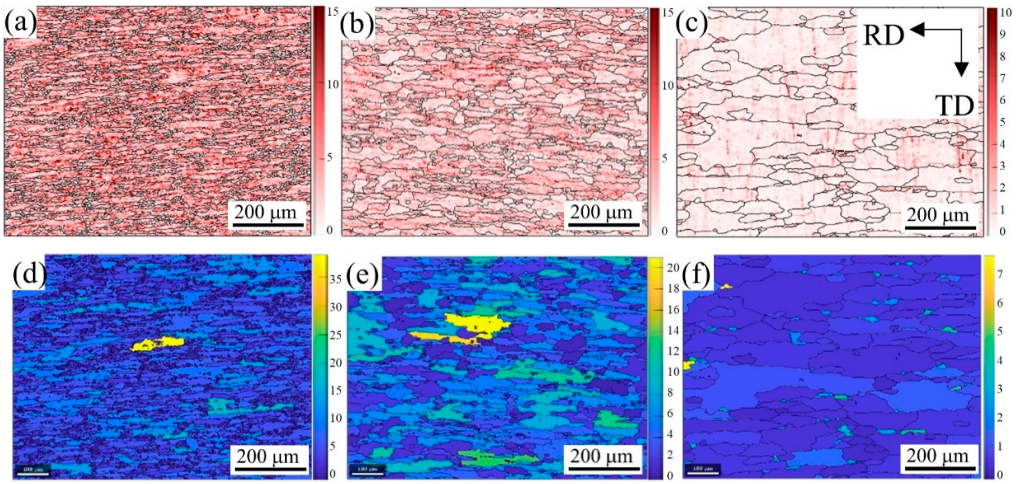

Figure 6. Kernel average misorientation results of 2A14 Al alloy on RD-TD plane annealing to (**a**) 505 ℃, (**b**) 555 ℃, (**c**) 580 ℃; Grain orientation spread maps of 2A14 Al alloy on RD-TD plane annealing to (d) 505 ℃, (e) 555 ℃, (f) 580 ℃.

In addition, there was a phenomenon of texture in the hot rolling structure. The micro-texture of the corresponding region can be characterized by analyzing the EBSD results. Figure 7(a)-(d) shows the pole figure of 2A14 alloy at hot-rolled stage, and annealing to 505 ℃, 555 ℃, and 580 ℃, respectively. The pole figures shows the distribution of texture in {100}, {110} and {111}. There was obvious texture phenomenon in the hot rolling structure (Figure 7(a)), and the intensity of texture was the highest at {100}, and the peak intensity of texture reached 9.36. With the increase of annealing temperature, the peak intensity of texture decreased. The peak intensity of texture was decreased to 5.56, 3.56, and 3.01 when annealed to 505 ℃, 555 ℃, and 580 ℃, respectively. At the same time, with the increase of annealing temperature, the preferred orientation gradually changed to random orientation.

Preprints (www.preprints.org) | NOT PEER-REVIEWED | Posted: 27 February 2023 doi:10.20944/preprints202302.0436.v1

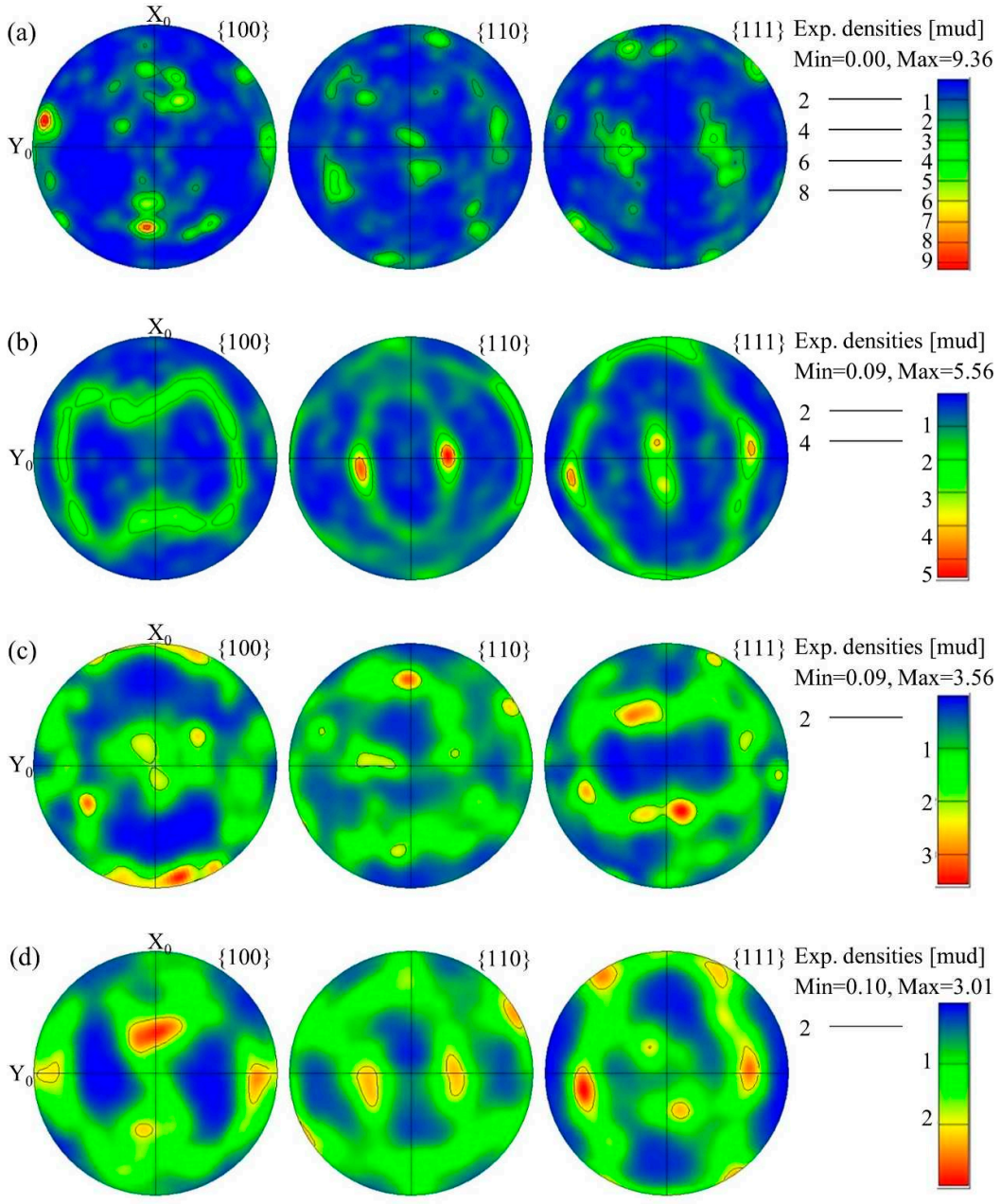

Figure 7. {100}, {110}, and {111} pole figures of 2A14 Al alloy: (**a**) hot-rolled state, annealing to (**b**) 505 ℃, (**c**) 555 ℃, (**d**) 580 ℃.

In order to calibrate the type of texture, the corresponding orientation distribution function (ODF) maps was drawn. The ODF maps were displayed with φ_2 is constant value at an interval of 5°. The ODF maps of hot-rolled, annealed to 505 ℃, 555 ℃, and 580 ℃ is shown in Figure 8 (a)-(d), respectively. The intensity of texture was highest at the hot-rolled state, which reached 13.208. With the increase of annealing temperature, the intensity of texture gradually decreased. The intensity of texture decreased to 5.539, 4.549, and 4.437 when annealed to 505 ℃, 555 ℃, and 580 ℃, respectively. Table 2 shows some of the common texture types that appear in this study [20,21]. According to the way of formation, texture can be divided into deformation texture and recrystallization texture [22–24]. A mixed texture was appeared at the hot-rolled state (Figure 8(a)). Texture with the highest intensity was the recrystallized P texture with {011} <122>. Second high intensity texture was the recrystallized brass texture with {236} <385>. And three deformation texture in order of intensity were

Preprints (www.preprints.org) | NOT PEER-REVIEWED | Posted: 27 February 2023 doi:10.20944/preprints202302.0436.v1

copper texture with {112} <111>, brass texture with {011} <211>, S texture with {123} <634>, respectively. With the increase of annealing temperature, these textures appeared in the subsequent annealing process, but the intensity of texture changed. The peak intensity of ODF maps was gradually decreasing, indicating that the texture intensity was decreasing with the increase of annealing temperature, whether deformation texture or recrystallization texture. In addition, with the increase of annealing temperature, the texture type changes from the mixed texture type of deformation texture and recrystallization texture to the mixed texture type dominated by recrystallization texture. These also show that in the process of recrystallization, the microstructure gradually changed from preferred orientation to random orientation, but the recrystallization texture was inherited in the process of transformation, and the strength gradually decreased.

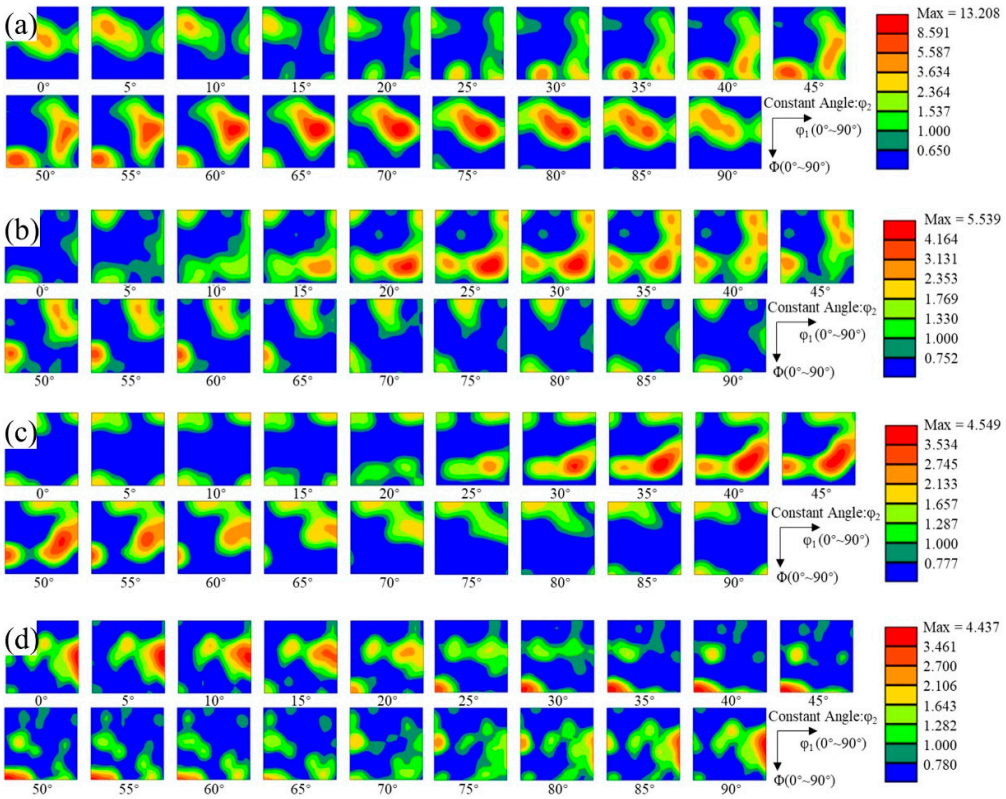

Figure 8. Orientation distribution function (ODF) maps with the φ_2 is constant value and the interval is 5° of 2A14 Al alloy: (**a**) hot-rolled, annealed to (**b**) 505 ℃, (**c**) 555 ℃, (**d**) 580 ℃.

Table 2. Main texture in hot-rolled 2A14 Al alloy is a table.

Texture type	Texture name	{hkl}<uvw>(φ_1, Φ, φ_2)
Deformation texture	Copper	{112}<111> (90, 35, 45)
	Brass	{011}<211> (35, 45, 0)
	S	{123}<634> (59, 37, 63)
Recrystallization texture	P	{011}<122> (70, 45, 0)
	Recrystallized brass	{236}<385> (79, 31, 33)

In addition, the analysis of misorientation axis can also explain the change of texture during recrystallization annealing. Figure 9 shows the misorientation axis figure and the corresponding distribution of misorientation axis figure annealed to 505 ℃, 555 ℃, and 580 ℃, respectively. With the increase of temperature, the density of misorientation axis decreased gradually. The highest intensity of misorientation axis was [001] annealed to 505 ℃. When the annealing temperature rose

Preprints (www.preprints.org) | NOT PEER-REVIEWED | Posted: 27 February 2023 doi:10.20944/preprints202302.0436.v1

to 555 ℃, the highest intensity of misorientation axis turned to [$\bar{1}$11], the misorientation axis in [001] still existed, but the intensity decreased greatly. When the annealing temperature rose to 580 ℃, the misorientation axis in [001] disappeared. In general, the density of the misorientation axis decreased, which was consistent with the previous results, indicating that the microstructure changed from preferred orientation to random orientation during recrystallization annealing, but the recrystallization texture was retained and the deformation texture tended to disappear.

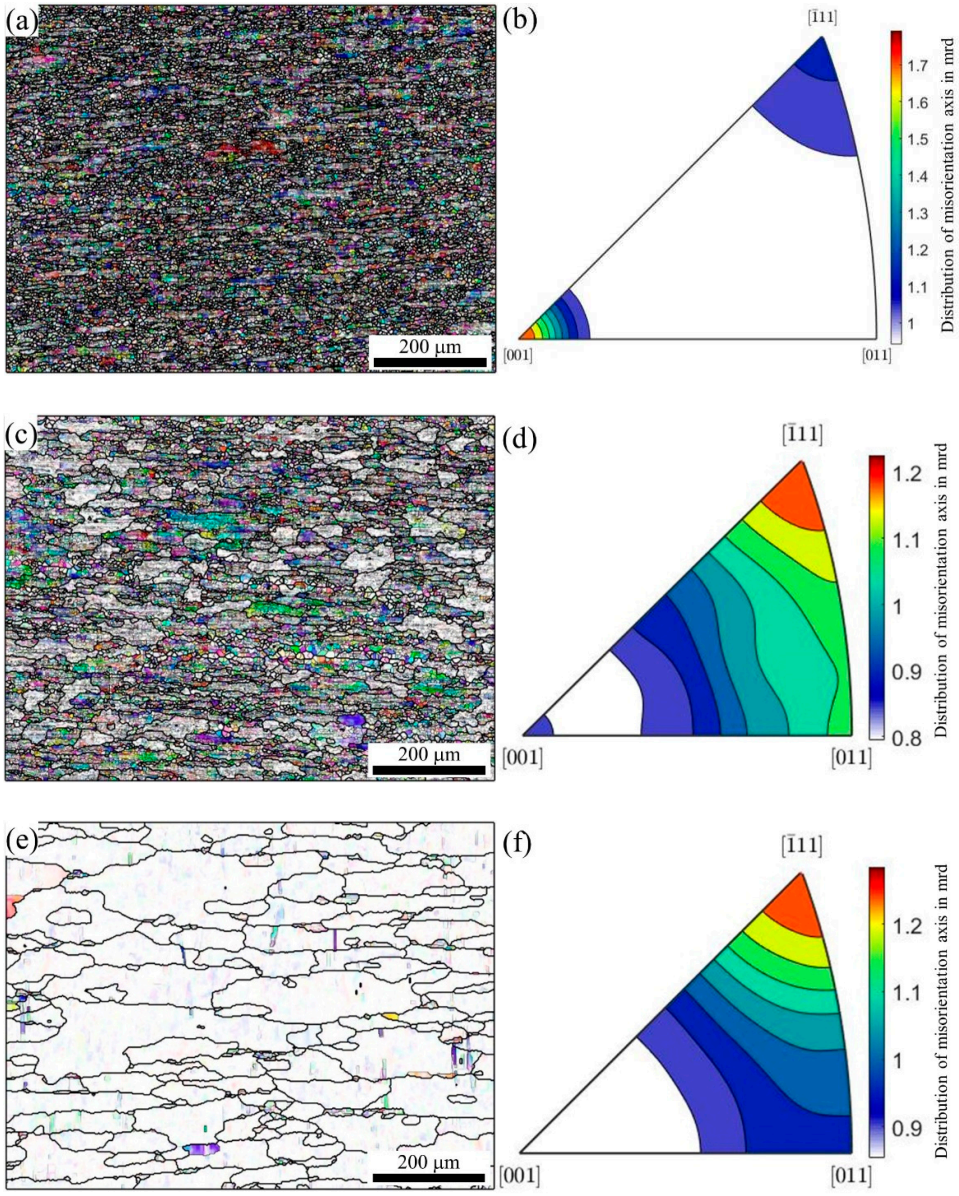

Figure 9. The misorientation axis in crystal coordinates and corresponding distribution of misorientation axis: (**a**), (**b**) 505 ℃, (**c**), (**d**) 555 ℃, (**e**), (**f**) 580 ℃.

3.3. Second-phase particles in 2A14 alloy

The results of EBSD show that recovery and recrystallization occur during recrystallization annealing. At 555 ℃, the LAGBs in some grains can migrate, while the LAGBs in most grains have no obvious migration. It is inferred that the migration of LAGBs is hindered by the second phase particles, so it is necessary to detect the phase and element distribution in the 2A14 Al alloy. Figure

Preprints (www.preprints.org) | NOT PEER-REVIEWED | Posted: 27 February 2023 doi:10.20944/preprints202302.0436.v1

10 shows the X-ray diffraction (XRD) patterns of the 2A14 Al alloy at hot-rolled stated and annealed to 505, 555, 580 ℃, respectively. The diffraction peaks of the four patterns occurred at 2θ of 38.47°, 44.74°, 65.13°, 78.23°, 82.46°, which corresponded to the diffraction of (111), (200), (220), (311), and (222) planes of the Al matrix phase, respectively. And the weaker diffraction peaks of the four patterns occurred at 2θ of 20.62°, 37.87°, 45.59°, 47.33°, 47.81°, which corresponded to the diffraction of (110), (211), (112), (310), (202) planes of the θ-Al2Cu phase, respectively. It is difficult to observed phases other than Al matrix and θ phase in the XRD patterns, but this does not mean that there were only two phases in the alloy. Because the absolute proportion of other phases was too low to observe by XRD. The characterization of other phases will be given in the later SEM and TEM results. The diffraction peak intensity of θ phase was the same at hot-rolled stated and annealed to 505 ℃, but decreased when annealed to 555 ℃, and nearly disappeared when annealed to 580 ℃, which indicates that θ phase was dissolved in the Al matrix, that is, solid solution phenomenon occurred at 555 ℃. This is consistent with the DSC results that there was the dissolution endothermic peak of θ phase at 520 ℃ (Figure 1). In addition, the relative intensity of diffraction peaks on different crystal planes of Al matrix also evolve during annealing. For example, the diffraction peak of Al matrix at 2θ of 38.47° corresponding the (111) plane of Al matrix first increased and then decreased with the increase of annealing temperature. The diffraction peak of Al matrix at 2θ of 82.46° corresponding the (222) plane of Al matrix almost disappeared when annealed to 580 ℃. The results show that the micro-texture evolved during annealing process, and the crystal plane evolved from preferred orientation to random orientation, which is consistent with the results of PF (Figure 7) and ODF (Figure 8) diagram in EBSD.

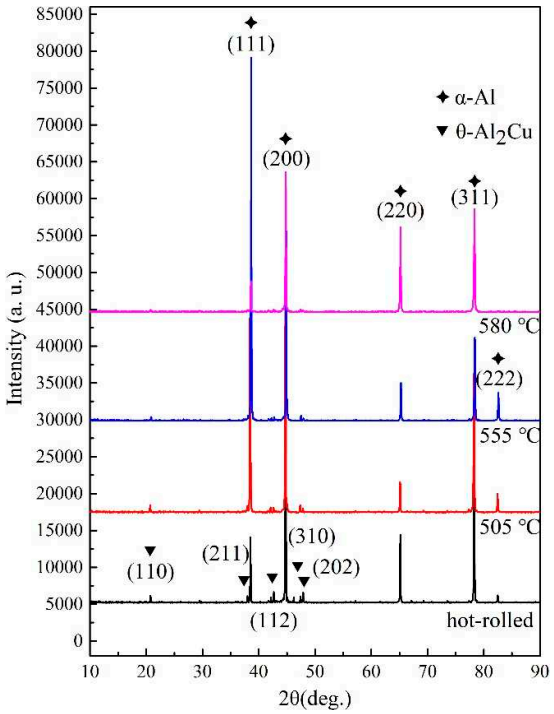

Figure 10. XRD result of the 2A14 aluminum alloy at hot-rolled stated and annealing to 505 ℃, 555 ℃ and 580 ℃.

Figure 11 shows the distribution of elements in the 2A14 Al alloy at different scales. Figure 11 (a) shows the high-angle annular dark-field (HAADF) scanning transmission at higher magnification of 2A14 Al alloy annealed to 555 ℃. In the figure, precipitates are dispersed in the sub-grains. Figure 11(b) is the corresponding scanning map distribution diagram of the elements. It can be seen from Figure 11(b) that the second phase particles are dispersed in the sub-grains. Among them, the larger dispersed precipitate phase was Fe-Mn dispersed phase, and the smaller dispersed phase was Si

 doi:10.20944/preprints202302.0436.v1

phase, Mg-Zn phase and G-P zone formed by very small-scale enrichment of Cu element. The size of these dispersed precipitates was small enough to hinder the migration of sub-grain boundaries, LAGBs and dislocation slip during recrystallization annealing, which was usually called the pinning effect of second phase particles. Figure 11(c) shows the backscattered electron (BSE) map of SEM image at lower magnification. The contrast of BSE can well reflect the difference of atomic number of elements. Scanning at a small magnification shows that coarse second phases were distributed along the HAGBs. According to the corresponding element scanning distribution diagram, the coarse second phases were mainly Cu rich phase, Fe-Mn phase and Si rich phase.

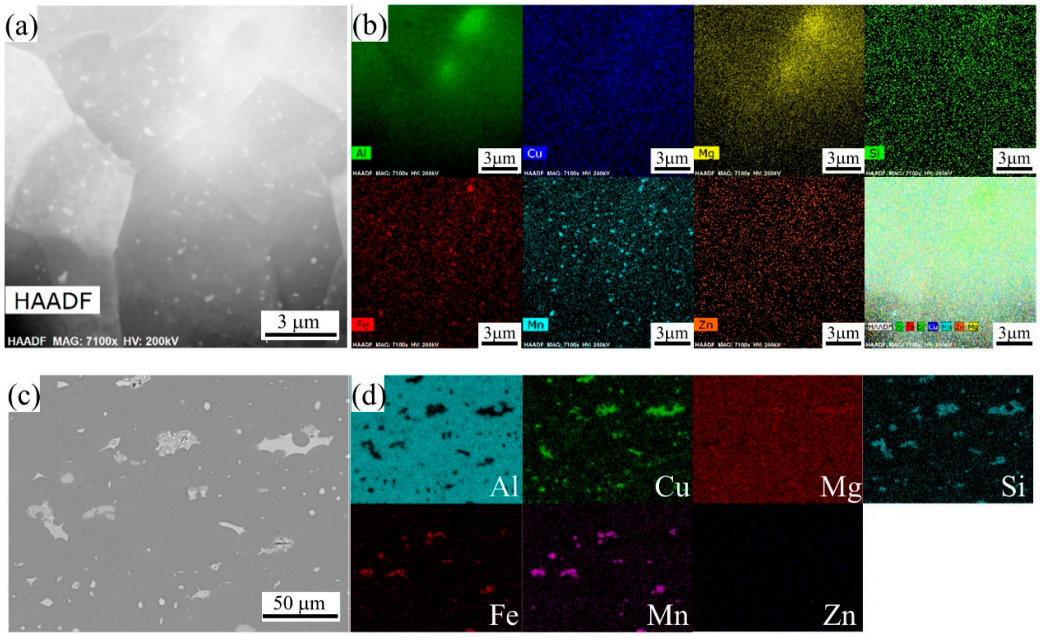

Figure 11. STEM images of 2A14 alloy annealing to 555 ℃: (**a**) the HAADF image of the precipitates, (**b**) the EDS mapping images of the main alloying elements; (**c**) The SEM images of 2A14 alloy, backscattered electron map and (**d**) the corresponding EDS mapping images of the main alloying elements.

3.4. Microstructure with smaller hierarchy of scale

Characterization of EBSD is limited to the relatively low magnification of SEM, and the smallest hierarchy of crystal defect that can be distinguished is LAGBs. EBSD is weak for characterization of microstructure at the scale of the dislocation substructure. Therefore, in order to better understand the evolution of smaller defects in the annealing process, it is necessary to characterize smaller defects such as sub-grain, sub-grain boundary (dislocation walls) by TEM. Although in the TEM at higher magnification, due to the small field of view, the characteristics of the local area cannot reflect the characteristics of the overall material, a more typical area can still be selected to represent the characteristics of the overall material. Figure 12 (a) and (b) shows the TEM image of 2A14 Al annealed to 505 ℃ with different magnification. It can be seen that there were a large number of slip bands, high-density dislocations and dislocation walls (sub-grain boundaries) formed by the directional arrangement of dislocations in the sub-grains. The cells formed by grain subdivision or fragmentation were separated by dislocation walls. This shows that there was not obvious recrystallization phenomenon when annealing to 505 ℃, and even the annealing recovery phenomenon was not obvious. In addition, it can be found that there were insoluble particles in the cells and the phenomenon of pinning dislocations by insoluble particles. The typical TEM image of 2A14 Al annealed to 555 ℃ are shown in Figure 12 (c). The dislocation density in most regions was lower than that annealed to 505 ℃, and some precipitated second phases can be seen in the cell and near the sub-grain boundary. The typical TEM image of 2A14 Al annealed to 580 ℃ are shown in Figure

Preprints (www.preprints.org) | NOT PEER-REVIEWED | Posted: 27 February 2023 doi:10.20944/preprints202302.0436.v1

12 (d). The size of the precipitated second phases were smaller than that annealed to 555 ℃. At 580 ℃, it is obvious that the second phases should have been dissolved into the matrix. Therefore, the precipitated phases in Figure 12 (d) was a finer precipitated phase secondary precipitated after sample preparation and quenching to room temperature, which was a phenomenon caused by sample preparation problems. The defects of dislocations sub-grain boundaries were minimized when annealed to 580 ℃.

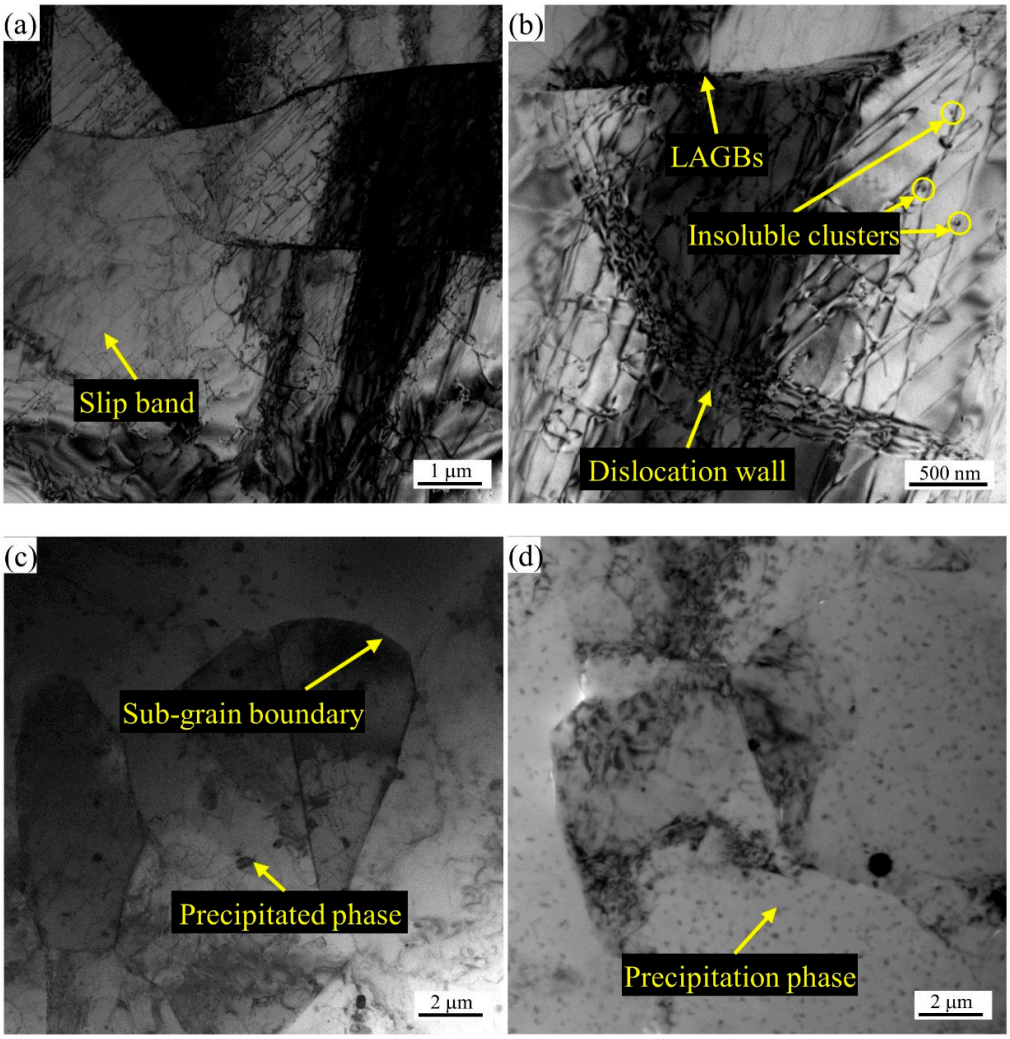

Figure 12. TEM bright field images of the 2A14 alloy annealing to (**a**) and (**b**) 505 ℃, (**c**) 555 ℃, (**d**) 580 ℃.

4. Discussion

4.1. The deformed state

The starting material was a hot-rolled thick plate of 2A14 alloy. Before the semi-solid annealing experiment, the raw material had gone through the hot rolling process with a cumulative deformation of 90% at 400 ℃. In the process, on the one hand, the deformation energy was stored in the microstructure in the form of various crystal defects; On the other hand, with the input of heat, the softening process of dynamic recovery (DRV) and dynamic recrystallization (DRX) also occurred. Huang and Logé [18] introduced in detail the classification of various dynamic recrystallization (DRX) mechanisms based on phenomenology. And many factors that affect the DRX mechanism including the stacking fault energy (SFE), the TMP conditions, the distribution of grain size, the

chemical composition of second phase, the distribution and size of the second phase etc. [25]. It is well known that Al is a face centered cubic (FCC) close packed structure with high SFE [26,27]. When subjected to large plastic deformation such as extrusion or rolling, metals with high SFE tend to facilitate cross-slip to form substructures like cells or sub-grains in the formation of dislocation cell subdivision rather than twinning and twin fragmentation [25,28]. The present findings seem to be consistent with other research which found the deformation characteristics in hot-rolled 2A14 alloy were dislocation cross-slip to form dislocation cells and sub-grains, which existed in the form of high-density LAGBs in EBSD results (Figure 5). Cells or sub-grains with high density of LAGBs were the characteristic result of typical DRV and continuous dynamic recrystallization (CDRX). As stated by Sakai et al. [29], Al alloys with high SFE were more prone to CDRX and DRV under the condition of large plastic deformation, resulting in ultra-fine grains. DRV and CDRX often occurred simultaneously, and high strain rate would promote the occurrence of CDRX. In addition, a few fine recrystallized (RXed) grains existed in the hot-deformation structure (Figure 3(c)), which is the characteristic result of typical discontinuous dynamic recrystallization (DDRX). As Huang and Logé [18] pointed out that, coarse second particles can accelerate DDRX by particle stimulated nucleation (PSN), which is consistent with the results in this study, the coarse second phase along the HAGBs provided the condition for DDRX nucleation. Besides, Hu et al. [30] pointed out that the dispersed fine particles tend to hinder boundary motion and slow down the CDRX process, also known as the Zener drag effect, which can be expressed as Eq. (2):

$$P \propto \gamma_{GB} \cdot {}^{V_f}/_{\bar{r}} , \quad (2)$$

where P is the Zener pressure, γ_{GB} is the grain boundary energy, V_f is the volume fraction of the particle and $\bar{r}$ is the mean size of the particles. The present findings seem to be consistent with the above description, dispersed fine second phase hinder the migration of LAGBs (Figure 11 (a) and (b)). Therefore, there was a mixed softening mechanism of DRV, CDRX, and DDRX during the hot rolling process of 2A14 Al alloy. High SFE promote the DRV and CDRX, while because of the PSN and Zener drag effect, DDRX mechanism also existed in the hot-rolled 2A14 Al alloy.

4.2. The second phases in 2A14 Al alloy

The second phases in alloy are mainly determined by the alloy composition, while the size and distribution state of second phase was affected by both TMP conditions and the heat treatment process. The 2A14 alloy can be strengthened by standard solid solution (SS) and artificial aging treatment. The strengthening phase is mainly the transition phase θ'' and θ' of the equilibrium phase θ-Al_2Cu. The aging precipitation sequence of 2A14 Al alloy can be expressed as: Al (super saturated solid solution) → {atomic clusters (Al, Cu)} → {G-P zones} → {transition θ'' phase precipitates} → {transition θ' phase precipitates} → {equilibrium θ-Al_2Cu}[9,10,31–33]. The hot-rolled state used in this study can be regarded as T4 heat treatment state. That was a certain solid solution after hot rolling and quenching, and then it was stored at room temperature for a long time as natural aging state. There were atomic clusters (Al,Cu) and G-P zones in the alloy as shown in Figure 12(b). And the insoluble particles in Figure 12 (a) and (b) were considered to be atomic clusters (Al, Cu) and G-P zones of Al-Cu according to the results reported by Han et al. [34]. The transition phase θ'' and θ' were the smallest phase in hot-rolled 2A14 Al alloy that will play a pinning role in dislocation, which will inhibit the annihilation of dislocation and then inhibit the nucleation of continuous recrystallization. In previous studies, the strengthening effect of the transition phase on the alloy caused by the inhibition of dislocation slip is often emphasized, but the effect of the transition phase on recrystallization is rarely discussed. Jiao et al. [35] reported the atomic-scale structure of transition β'' and β' phases, the atomic-scale structure of aging precipitates is small enough to hinder the slip of dislocation. Ding et al. [36] reported the pinning effect of aging precipitated particles on the migration of LAGBs, and found that aging precipitated particles inhibited the static recovery of A5083 aluminum alloy.

In addition to the aging precipitates, there were a larger size of precipitates content of Fe, Mn and Si as shown in Figure 11(a) and (b). Fe and Si elements are inevitably introduced into the

metallurgy process of commercial alloys, which is easy to form hard and brittle intermetallic phases like Fe_3Al, AlFeSi, etc. and weaken the properties of the alloy [37,38]. Generally, Mn element will be added to aluminum alloy to form soft solid solution $MnAl_6$ phase to dissolve Fe element and Si element and form (Mn,Fe)Al_6 or Al(MnFeSi) [39–41]. However, 2A14 alloy is mainly composed of Al matrix phase, and the relative volume fraction of other phases was low to detect by XRD (Figure 10). Therefore, in this study, only Al matrix phase and eutectic coarse phase θ-Al_2Cu precipitated along grain boundary can be identified by XRD results (Figure 10). The dispersed fine precipitates in Figure 11 (a) and (b) were considered to be (Mn, Fe)Al_6 or Al(MnFeSi) according to the results provided by Engler et al. [39–41]. In addition, Qian et al. reported the effects of Mn content on the recrystallization resistance of aluminum alloys [42]. The results showed that with addition of Mn, numerous dispersed Al(Mn,Fe)Si phase generated, exhibited obvious resistance on recrystallization compared with base alloy free of Mn and dispersoids. For the second phase of this size, it will have obvious Zener pinning effect on the interface such as LAGBs and HAGBs, the Zener pressure can be expressed by Eq. (2). Kuang et al. [43] reported the Zener pinning pressure on the migration of grain boundary that cast Al-Mn-Fe-Si alloy, the alloy was resistant to recrystallization and stable up to a temperature of 550 ℃. Hu et al. [44] emphasized that solute-drag and Zener pinning effect retarded recrystallization and grain growth during annealing process.

The largest second phase was the coarse particles of eutectic equilibrium θ phase precipitated at HAGBs, as shown in the EDS results in Figure 11 (c) and (d) and the XRD pattern in Figure 10. Wang et al. [45] reported the directional solidification of Al-Cu alloy, the solute distribution of eutectic equilibrium θ phase was infected by the thermoelectric magnetic field and the eutectic θ phase precipitated at HAGBs. As reported by Huang and Logé [18], coarse second phase often acts as the heterogeneous nucleation point of recrystallization and promotes the recrystallization process via PSN mechanism. She et al. [46] investigated the relationship of PSN on the recrystallization of hot-extruded 7055 aluminum alloy, and founded that coarse second phase particles were more liable to induce PSN recrystallization and produce PSN recrystallized grains with random orientations. In addition, coarse second phase particles had a pinning effect on the migration of HAGBs that inhibit the grain growth during annealing.

4.3. The recrystallization mechanism

In order to more intuitively describe the recrystallization behavior of hot-rolled 2A14 aluminum during semi-solid annealing, the schematic diagram of recrystallization mechanism of the process is drawn, as shown in Figure 13. The whole process can be described in three stages: the hot-rolled microstructure state at room temperature, the recrystallization homogeneous nucleation state when continuously heating up to near solidus temperature, and the static recrystallized (SRXed) state after heating up to semi-solid temperature. The hot-rolled state of 2A14 Al alloy at room temperature (RT) had a complex microstructure. The grains were elongated along the rolling direction. The coarse second phase precipitates at HAGBs (equilibrium θ- Al_2Cu phase). At the same time, there are dynamic recrystallized grains near the coarse second phase. Wang et al. [47] studied the DRX and phase distribution of 7075 aluminum alloy during hot extrusion. The results show that the microstructure was richer in scale hierarchy under hot deformation by CDRX mechanism, and the second phases were easier to refine and distribute in the microstructure under thermoplastic deformation. Behnamfard et al. [48] investigated the hot-rolling process of aluminum matrix nanocomposite, and founded that hot rolling process improved the mechanical properties of nanocomposites probably because the ultra-fine grain structure formed by hot rolling has interactive strengthening effect with nano-ceramics.

Preprints (www.preprints.org) | NOT PEER-REVIEWED | Posted: 27 February 2023 doi:10.20944/preprints202302.0436.v1

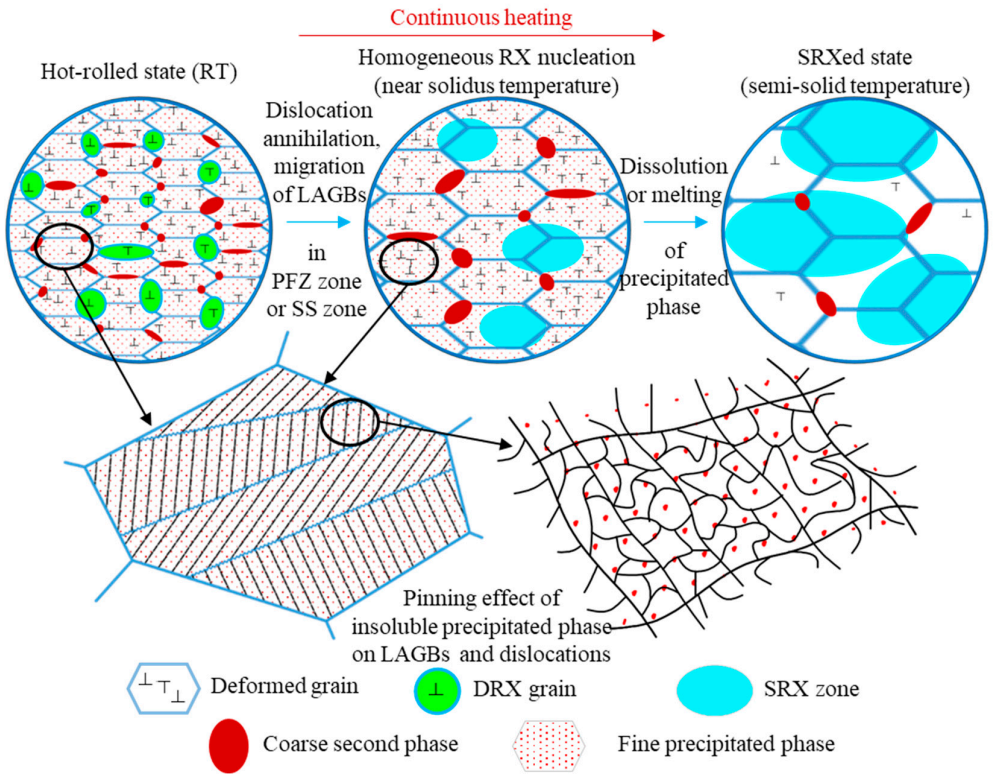

Figure 13. Schematic diagram of the recrystallization mechanism during semi-solid annealing of hot-rolled 2A14 Al alloy.

When the hot-rolled structure was annealed to solid-state high temperature, firstly, the grain size grows under the migration of large angle grain boundary, while the grain growth speed is slow due to the pinning effect of coarse second phase on HAGBs. Homogeneous recrystallization occurred in some regions, that is, the annihilation of dislocation and the migration of small angle grain boundary produce low-density grain boundary regions. The dislocation density in most areas was still very high, and the density of LAGBs was still very high. This was because there were fine precipitates in the grains, Zener drag effect hinder the migration of LAGBs, and there were atomic clusters (Al, Cu) and G-P zones that hinder the slip of dislocations. Hence, it could be conceivably hypothesized that the homogeneous nucleation zone was the precipitation free zones (PFZs), or there was a certain temperature fluctuation in the homogeneous nucleation zone, which made the second phase particles and atomic clusters dissolve in the matrix. Chen et al. [49] investigated the precipitation behavior of Al-Cu-Mg aluminum alloy, and found that excessive Mg resulted in the formation of PFZs, which support the hypothesis that homogeneous nucleation zone happened in the PFZs in 2A14 alloy. Wei et al. [50] also reported the irregular and uniform PFZs appeared in Al-Mg-Si alloy after aging process which support the hypothesis. The report on PFZs also supports this conjecture results of Han et al. [34] on the aging precipitates of Al-Cu aluminum alloy.

When the annealing temperature reached the semi-solid temperature, the dispersed fine precipitates were dissolved in the matrix, the insoluble atomic clusters are dissolved, the pinning effect on LAGBs and the blocking effect on the dislocation slip disappeared, the dislocations in the microstructure were annihilated, and the migration of LAGBs reduced the density of the LAGBs. The coarse second phase melted partially, the barrier effect on large angle grain boundary migration decreased, and the grain grew rapidly.

5. Conclusions

In this paper, the SRX process of hot-rolled 2A14 Al alloy during continuous heating to the semi-solid temperature was investigated. XRD, EBSD and TEM methods were applied to analyze the phase

distribution, microstructure and the SRX mechanism from various perspectives and various scale hierarchy. The following conclusions can be drawn:

(1) The obvious recrystallization nucleation process occurred only when the temperature rose to near solidus temperature, and the recrystallization process mainly occurs after the temperature rises to semi-solid temperature. The recrystallization mechanism was dominated by CSRX. With the increase of annealing temperature, the grains grew slowly. After reaching the semi-solid temperature, the grains grew rapidly.

(2) Recrystallization did not occur until the annealing temperature reached near the solidus because of the Zener drag effect of the dispersed precipitates on LAGBs and the blocking effect of atomic clusters on dislocation slip. The homogeneous recrystallization nucleates in the PFZs or the pre-dissolution zone of precipitates/atomic clusters.

(3) With the process of semi-solid annealing, the deformation texture fraction in micro-texture decreased, while the recrystallization texture fraction increased, and the micro-texture changed from preferred orientation to random orientation.

Author Contributions: Conceptualization, J.J. and Y.W.; methodology, Y.L.; software, Y.L.; validation, Y.Z., M.H. and J.D.; formal analysis, Y.L.; investigation, Y.L.; resources, J.J.; data curation, Y.L.; writing—original draft preparation, Y.L.; writing—review and editing, Y.Z., M.H. and J.D.; visualization, Y.L.; supervision, J.J.; project administration, J.J.; funding acquisition, J.J. All authors have read and agreed to the published version of the manuscript.

Funding: This research was funded by the National Natural Science Foundation of China (NSFC) under Grant No.U2241232 and the National Key R&D Program of China (No.2019YFB2006503).

Institutional Review Board Statement: Not applicable.

Informed Consent Statement: Informed consent was obtained from all subjects involved in the study. Written informed consent has been obtained from the patient(s) to publish this paper applicably.

Data Availability Statement: The data presented in this study are available on request from the corresponding author.

Acknowledgments: This work was supported by the National Natural Science Foundation of China (NSFC) under Grant No.U2241232 and the National Key R&D Program of China (No.2019YFB2006503).

Conflicts of Interest: The authors declare no conflict of interest.

References

1. Santos, M.C.; Machado, A.R.; Sales, W.F.; Barrozo, M.A.S.; Ezugwu, E.O. Machining of Aluminum Alloys: A Review. *The International Journal of Advanced Manufacturing Technology* **2016**, *86*, 3067–3080, doi:10.1007/s00170-016-8431-9.
2. Williams, J.C.; Starke, E.A. Progress in Structural Materials for Aerospace Systems11The Golden Jubilee Issue—Selected Topics in Materials Science and Engineering: Past, Present and Future, Edited by S. Suresh. *Acta Materialia* **2003**, *51*, 5775–5799, doi:10.1016/j.actamat.2003.08.023.
3. Gregson, P.J. Aluminium Alloys: Physical Metallurgy, Processing and Properties. In *High Performance Materials in Aerospace*; Flower, H.M., Ed.; Springer Netherlands: Dordrecht, 1995; pp. 49–84 ISBN 978-94-011-0685-6.
4. Flemings, M.C. Behavior of Metal Alloys in the Semisolid State. *Metallurgical Transactions A* **1991**, *22*, 957–981, doi:10.1007/BF02661090.
5. Czerwinski, F. Thermomechanical Processing of Metal Feedstock for Semisolid Forming: A Review. *Metallurgical and Materials Transactions B* **2018**, *49*, 3220–3257, doi:10.1007/s11663-018-1387-4.
6. Binesh, B.; Aghaie-Khafri, M. RUE-Based Semi-Solid Processing: Microstructure Evolution and Effective Parameters. *Materials & Design* **2016**, *95*, 268–286, doi:10.1016/j.matdes.2016.01.117.
7. Fu, J.; Wang, S.; Wang, K. Influencing Factors of the Coarsening Behaviors for 7075 Aluminum Alloy in the Semi-Solid State. *Journal of Materials Science* **2018**, *53*, 9790–9805, doi:10.1007/s10853-018-2246-z.
8. Jiang, J.; Liu, Y.; Xiao, G.; Wang, Y.; Xiao, X. Effects of Temperature and Time on Microstructural Evolution of Semisolid 5A06 Aluminum Alloy: Preparation of Semisolid Billets in Ellipsoid Solid Phase. *Journal of Materials Engineering and Performance* **2020**, *29*, 5346–5359, doi:10.1007/s11665-020-04959-8.
9. Lan, J.; Shen, X.; Liu, J.; Hua, L. Strengthening Mechanisms of 2A14 Aluminum Alloy with Cold Deformation Prior to Artificial Aging. *Materials Science and Engineering: A* **2019**, *745*, 517–535, doi:10.1016/j.msea.2018.12.051.

10. Wang, M.; Huang, L.; Liu, W.; Ma, Y.; Huang, B. Influence of Cumulative Strain on Microstructure and Mechanical Properties of Multi-Directional Forged 2A14 Aluminum Alloy. *Materials Science and Engineering: A* **2016**, *674*, 40–51, doi:10.1016/j.msea.2016.07.072.
11. Wang, B.; Yi, Y.; He, H.; Huang, S. Effects of Deformation Temperature on Second-Phase Particles and Mechanical Properties of Multidirectionally-Forged 2A14 Aluminum Alloy. *Journal of Alloys and Compounds* **2021**, *871*, 159459, doi:10.1016/j.jallcom.2021.159459.
12. Chen, G.; Chen, Q.; Qin, J.; Du, Z. Effect of Compound Loading on Microstructures and Mechanical Properties of 7075 Aluminum Alloy after Severe Thixoformation. *Journal of Materials Processing Technology* **2016**, *229*, 467–474, doi:10.1016/j.jmatprotec.2015.10.005.
13. Chen, Q.; Chen, G.; Ji, X.; Han, F.; Zhao, Z.; Wan, J.; Xiao, X. Compound Forming of 7075 Aluminum Alloy Based on Functional Integration of Plastic Deformation and Thixoformation. *Journal of Materials Processing Technology* **2017**, *246*, 167–175, doi:10.1016/j.jmatprotec.2017.03.023.
14. Jiang, J.; Wang, Y.; Xiao, G.; Nie, X. Comparison of Microstructural Evolution of 7075 Aluminum Alloy Fabricated by SIMA and RAP. *Journal of Materials Processing Technology* **2016**, *238*, 361–372, doi:10.1016/j.jmatprotec.2016.06.020.
15. Humphreys, J.; Rohrer, G.S.; Rollett, A. Chapter 1 - Introduction. In *Recrystallization and Related Annealing Phenomena (Third Edition)*; Humphreys, J., Rohrer, G.S., Rollett, A., Eds.; Elsevier: Oxford, 2017; pp. 1–11 ISBN 978-0-08-098235-9.
16. Huang, K.; Marthinsen, K.; Zhao, Q.; Logé, R.E. The Double-Edge Effect of Second-Phase Particles on the Recrystallization Behaviour and Associated Mechanical Properties of Metallic Materials. *Progress in Materials Science* **2018**, *92*, 284–359, doi:10.1016/j.pmatsci.2017.10.004.
17. Jiang, J.; Zhang, Y.; Wang, Y.; Xiao, G.; Liu, Y.; Zeng, L. Spheroidizing Process of 2A12 Aluminum Alloy Grains during Heating up and Semisolid Isothermal Treatment Stages. *Journal of Materials Engineering and Performance* **2021**, *30*, 5974–5986, doi:10.1007/s11665-021-05796-z.
18. Huang, K.; Logé, R.E. A Review of Dynamic Recrystallization Phenomena in Metallic Materials. *Materials & Design* **2016**, *111*, 548–574, doi:10.1016/j.matdes.2016.09.012.
19. Wang, Y.; Zhao, S.; Zhao, X.; Zhao, Y. Microstructural Coarsening of 6061 Aluminum Alloy Semi-Solid Billets Prepared via Recrystallization and Partial Melting. *Journal of Mechanical Science and Technology* **2017**, *31*, 3917–3923, doi:10.1007/s12206-017-0737-5.
20. Humphreys, J.; Rohrer, G.S.; Rollett, A. Chapter 3 - Deformation Textures. In *Recrystallization and Related Annealing Phenomena (Third Edition)*; Humphreys, J., Rohrer, G.S., Rollett, A., Eds.; Elsevier: Oxford, 2017; pp. 81–107 ISBN 978-0-08-098235-9.
21. Humphreys, J.; Rohrer, G.S.; Rollett, A. Chapter 12 - Recrystallization Textures. In *Recrystallization and Related Annealing Phenomena (Third Edition)*; Humphreys, J., Rohrer, G.S., Rollett, A., Eds.; Elsevier: Oxford, 2017; pp. 431–468 ISBN 978-0-08-098235-9.
22. Zhang, J.X.; Sun, H.Y.; Li, J.; Liu, W.C. Effect of Precipitation State on Recrystallization Texture of Continuous Cast AA 2037 Aluminum Alloy. *Materials Science and Engineering: A* **2019**, *754*, 491–501, doi:10.1016/j.msea.2019.03.107.
23. Chen, X.; Peng, Y.; Chen, C.; Li, J.; Wang, K.; Wang, T. Mechanical Behavior and Texture Evolution of Aluminum Alloys Subjected to Strain Path Changes: Experiments and Modeling. *Materials Science and Engineering: A* **2019**, *757*, 32–41, doi:10.1016/j.msea.2019.04.091.
24. Wang, X.; Shi, T.; Jiang, Z.; Chen, W.; Guo, M.; Zhang, J.; Zhuang, L.; Wang, Y. Relationship among Grain Size, Texture and Mechanical Properties of Aluminums with Different Particle Distributions. *Materials Science and Engineering: A* **2019**, *753*, 122–134, doi:10.1016/j.msea.2019.03.034.
25. McQueen, H.J. Development of Dynamic Recrystallization Theory. *Materials Science and Engineering: A* **2004**, *387–389*, 203–208, doi:10.1016/j.msea.2004.01.064.
26. Muzyk, M.; Pakiela, Z.; Kurzydlowski, K.J. Ab Initio Calculations of the Generalized Stacking Fault Energy in Aluminium Alloys. *Scripta Materialia* **2011**, *64*, 916–918, doi:10.1016/j.scriptamat.2011.01.034.
27. Gruber, B.; Grabner, F.; Falkinger, G.; Schökel, A.; Spieckermann, F.; Uggowitzer, P.J.; Pogatscher, S. Room Temperature Recovery of Cryogenically Deformed Aluminium Alloys. *Materials & Design* **2020**, *193*, 108819, doi:10.1016/j.matdes.2020.108819.
28. Huang, C.X.; Hu, W.; Yang, G.; Zhang, Z.F.; Wu, S.D.; Wang, Q.Y.; Gottstein, G. The Effect of Stacking Fault Energy on Equilibrium Grain Size and Tensile Properties of Nanostructured Copper and Copper–Aluminum Alloys Processed by Equal Channel Angular Pressing. *Materials Science and Engineering: A* **2012**, *556*, 638–647, doi:10.1016/j.msea.2012.07.041.
29. Sakai, T.; Belyakov, A.; Kaibyshev, R.; Miura, H.; Jonas, J.J. Dynamic and Post-Dynamic Recrystallization under Hot, Cold and Severe Plastic Deformation Conditions. *Progress in Materials Science* **2014**, *60*, 130–207, doi:10.1016/j.pmatsci.2013.09.002.
30. Hu, Y.L.; Lin, X.; Li, Y.L.; Zhang, S.Y.; Gao, X.H.; Liu, F.G.; Li, X.; Huang, W.D. Plastic Deformation Behavior and Dynamic Recrystallization of Inconel 625 Superalloy Fabricated by Directed Energy Deposition. *Materials & Design* **2020**, *186*, 108359, doi:10.1016/j.matdes.2019.108359.

31. Zhang, Y.; Yi, Y.; Huang, S.; Dong, F. Influence of Quenching Cooling Rate on Residual Stress and Tensile Properties of 2A14 Aluminum Alloy Forgings. *Materials Science and Engineering: A* **2016**, *674*, 658–665, doi:10.1016/j.msea.2016.08.017.
32. Wu, D.; Li, W.; Liu, K.; Yang, Y.; Hao, S. Optimization of Cold Spray Additive Manufactured AA2024/Al2O3 Metal Matrix Composite with Heat Treatment. *Journal of Materials Science & Technology* **2022**, *106*, 211–224, doi:10.1016/j.jmst.2021.07.036.
33. Liu, X.; Liu, Y.; Zhou, Z.; Zhan, Q. Enhanced Strength and Ductility in Al-Zn-Mg-Cu Alloys Fabricated by Laser Powder Bed Fusion Using a Synergistic Grain-Refining Strategy. *Journal of Materials Science & Technology* **2022**, *124*, 41–52, doi:10.1016/j.jmst.2021.12.078.
34. Han, T.; Wang, F.; Li, J.; He, C.; Zhao, N. Effect of GNPs on Microstructures and Mechanical Properties of GNPs/Al-Cu Composites with Different Heat Treatment Status. *Journal of Materials Science & Technology* **2021**, *92*, 1–10, doi:10.1016/j.jmst.2021.02.045.
35. Jiao, N.N.; Lai, Y.X.; Chen, S.L.; Gao, P.; Chen, J.H. Atomic-Scale Roles of Zn Element in Age-Hardened AlMgSiZn Alloys. *Journal of Materials Science & Technology* **2021**, *70*, 105–112, doi:10.1016/j.jmst.2020.09.009.
36. Ding, S.; Zhang, J.; Khan, S.A.; Yanagimoto, J. Static Recovery of A5083 Aluminum Alloy after a Small Deformation through Various Measuring Approaches. *Journal of Materials Science & Technology* **2022**, *104*, 202–213, doi:10.1016/j.jmst.2021.06.053.
37. Zhang, Y.; Jiang, J.; Wang, Y.; Xiao, G.; Liu, Y.; Huang, M. Recrystallization Process of Hot-Extruded 6A02 Aluminum Alloy in Solid and Semi-Solid Temperature Ranges. *Journal of Alloys and Compounds* **2022**, *893*, 162311, doi:10.1016/j.jallcom.2021.162311.
38. Atkinson, H.V.; Burke, K.; Vaneetveld, G. Recrystallisation in the Semi-Solid State in 7075 Aluminium Alloy. *Materials Science and Engineering: A* **2008**, *490*, 266–276, doi:10.1016/j.msea.2008.01.057.
39. Engler, O.; Kuhnke, K.; Hasenclever, J. Development of Intermetallic Particles during Solidification and Homogenization of Two AA 5xxx Series Al-Mg Alloys with Different Mg Contents. *Journal of Alloys and Compounds* **2017**, *728*, 669–681, doi:10.1016/j.jallcom.2017.09.060.
40. Engler, O.; Miller-Jupp, S. Control of Second-Phase Particles in the Al-Mg-Mn Alloy AA 5083. *Journal of Alloys and Compounds* **2016**, *689*, 998–1010, doi:10.1016/j.jallcom.2016.08.070.
41. Engler, O.; Liu, Z.; Kuhnke, K. Impact of Homogenization on Particles in the Al–Mg–Mn Alloy AA 5454 – Experiment and Simulation. *Journal of Alloys and Compounds* **2013**, *560*, 111–122, doi:10.1016/j.jallcom.2013.01.163.
42. Qian, X.; Parson, N.; Chen, X.-G. Effects of Mn Content on Recrystallization Resistance of AA6082 Aluminum Alloys during Post-Deformation Annealing. *Journal of Materials Science & Technology* **2020**, *52*, 189–197, doi:10.1016/j.jmst.2020.04.015.
43. Kuang, J.; Zhao, X.; Zhang, Y.; Zhang, J.; Liu, G.; Sun, J.; Xu, G.; Wang, Z. Impact of Thermal Exposure on the Microstructure and Mechanical Properties of a Twin-Roll Cast Al-Mn-Fe-Si Strip. *Journal of Materials Science & Technology* **2022**, *107*, 183–196, doi:10.1016/j.jmst.2021.07.022.
44. Hu, G.W.; Zeng, L.C.; Du, H.; Liu, X.W.; Wu, Y.; Gong, P.; Fan, Z.T.; Hu, Q.; George, E.P. Tailoring Grain Growth and Solid Solution Strengthening of Single-Phase CrCoNi Medium-Entropy Alloys by Solute Selection. *Journal of Materials Science & Technology* **2020**, *54*, 196–205, doi:10.1016/j.jmst.2020.02.073.
45. Wang, P.; Shuai, S.; Huang, C.; Liu, X.; Fu, Y.; Wang, J.; Ren, Z. Revealing the Influence of High Magnetic Field on the Solute Distribution during Directional Solidification of Al-Cu Alloy. *Journal of Materials Science & Technology* **2021**, *88*, 226–232, doi:10.1016/j.jmst.2021.01.058.
46. She, H.; Shu, D.; Dong, A.; Wang, J.; Sun, B.; Lai, H. Relationship of Particle Stimulated Nucleation, Recrystallization and Mechanical Properties Responding to Fe and Si Contents in Hot-Extruded 7055 Aluminum Alloys. *Journal of Materials Science & Technology* **2019**, *35*, 2570–2581, doi:10.1016/j.jmst.2019.07.014.
47. Wang, T.; Atehortua, J.E.; Song, M.; Reza-E-Rabby, M.; Taysom, B.S.; Silverstein, J.; Roosendaal, T.; Herling, D.; Whalen, S. Extrusion of Unhomogenized Castings of 7075 Aluminum via ShAPE. *Materials & Design* **2022**, *213*, 110374, doi:10.1016/j.matdes.2021.110374.
48. Behnamfard, S.; Taherzadeh Mousavian, R.; Khosroshahi, R.A.; Brabazon, D. A Comparison between Hot-Rolling Process and Twin-Screw Rheo-Extrusion Process for Fabrication of Aluminum Matrix Nanocomposite. *Materials Science and Engineering: A* **2019**, *760*, 152–157, doi:10.1016/j.msea.2019.05.109.

49. Chen, L.; Zhang, S.; Li, Z.; Zhao, G.; Zhang, C.; Lin, J. Investigation on Peripheral Coarse Grains and Precipitation Behavior of In-Situ TiB2/Al–Cu–Mg Composites with Various Mg Contents. *Materials Science and Engineering: A* **2021**, *826*, 142000, doi:10.1016/j.msea.2021.142000.
50. Wei, B.; Pan, S.; Liao, G.; Ali, A.; Wang, S. Sc-Containing Hierarchical Phase Structures to Improve the Mechanical and Corrosion Resistant Properties of Al-Mg-Si Alloy. *Materials & Design* **2022**, *218*, 110699, doi:10.1016/j.matdes.2022.110699.